Supporting Information

Bimetallic metal-organic framework glass as highly efficient bifunctional electrocatalyst for overall water splitting: the roles of metal sites

Song Xue[1], Fengliang Cao[1], Yin Huang[1], Shujin Hou[2], Xiying Fan[1,3,4,5,*]

[1]*Research Center on Advanced Chemical Engineering and Energy Materials, China University of Petroleum (East China), Qingdao 266580, China*

[2]*Department of Chemistry and Biochemistry and the Oregon Center for Electrochemistry, University of Oregon, Eugene, OR, 97403, USA*

[3]*CAS Key Laboratory of Biobased Materials, Qingdao Institute of Bioenergy and Bioprocess Technology, Chinese Academy of Sciences, No. 189, Songling Road, Qingdao 266101, China*

[4]*Shandong Energy Institute, No. 189, Songling Road, Qingdao 266101, China*

[5]*Qingdao New Energy Shandong Laboratory, No. 189, Songling Road, Qingdao 266101, China*

Corresponding author: fanxy@qibebt.ac.cn

1. Supplementary experimental section

X-ray absorption spectroscopy measurements: This beamline is connected to an undulator and equipped with two gratings that offer soft X-rays from 20 to 600 eV with a typical photon flux of 5×10^{10} photons/s and a resolution($E/\Delta E$) better than 10^5 at 29 eV. This system is comprised of four ultrahigh vacuum (UHV)chambers including analysis chamber, preparation chamber, molecular beam epitaxy (MBE) chamber, and a radial distribution chamber. The base pressures are 7×10^{-11}, 1×10^{-10}, 5×10^{-10} and 2×10^{-11} mbar, respectively. A sample load-lock system is connected to the sample transfer chamber. The analysis chamber is equipped with a VG Scienta R4000 analyzer, a monochromatic Al *Ka* X-ray source, a UV light source, low energy electron diffraction (LEED), a flood electron gun, and a manipulator with high precision and five-degree-of-freedom. The preparation chamber comprises an ion gun, a quartz crystal microbalance (QCM),a residual gas analyzer, a manipulator with high precision and four-degree-of-freedom, and several evaporators. The MBE chamber houses a QCM, several evaporators and a manipulator with two-degree-of-freedom. With this radial distribution chamber, the time for each transfer process between two chambers is less than 1 minute.

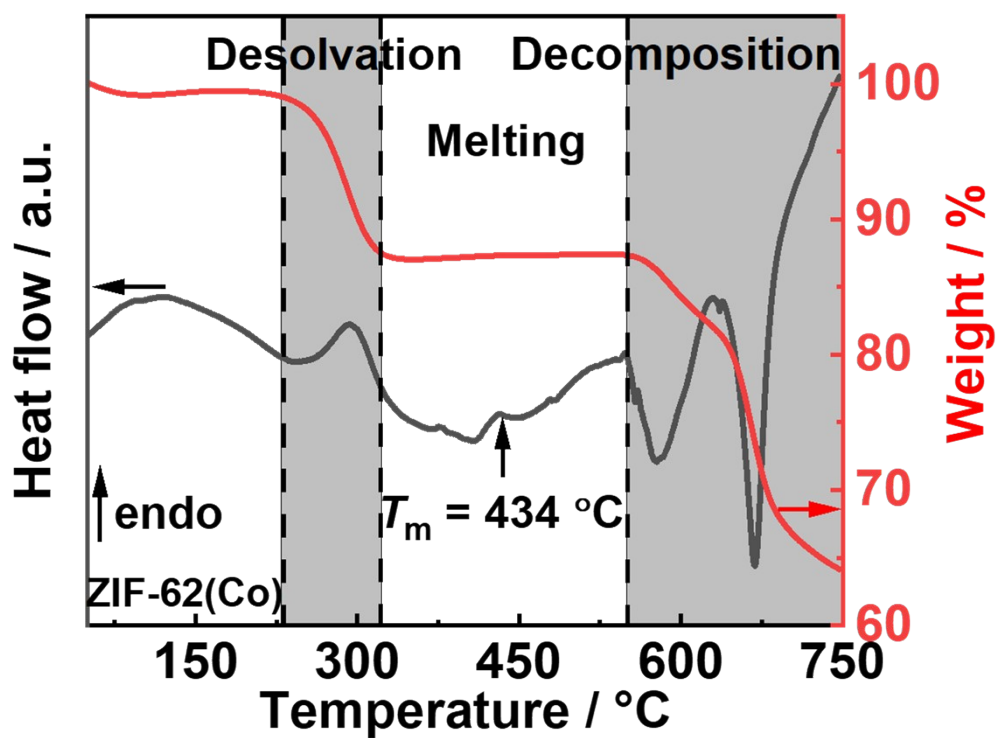## 2. Supplementary figures and tables

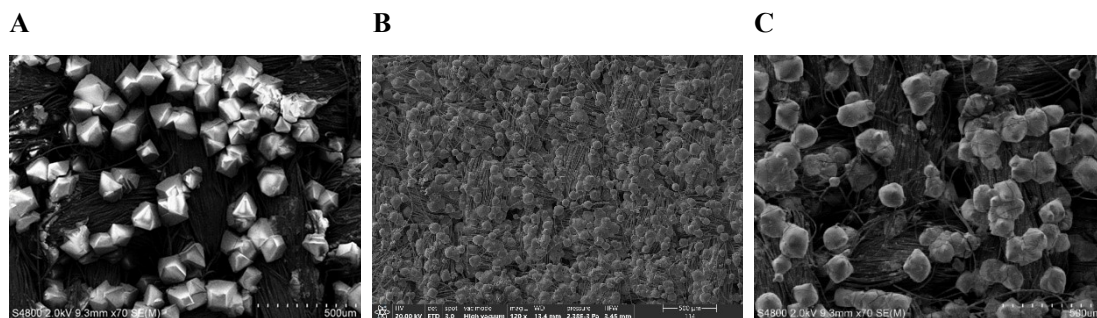**Figure S1** TG-DSC curve of the crystalline ZIF-62(Co).

Figure S2 SEM images of the crystalline ZIF-62(Co) (A), glassy ZIF-62(Co) (B), and glassy ZIF-62(Co)-Ni (C) on the carbon fibers.
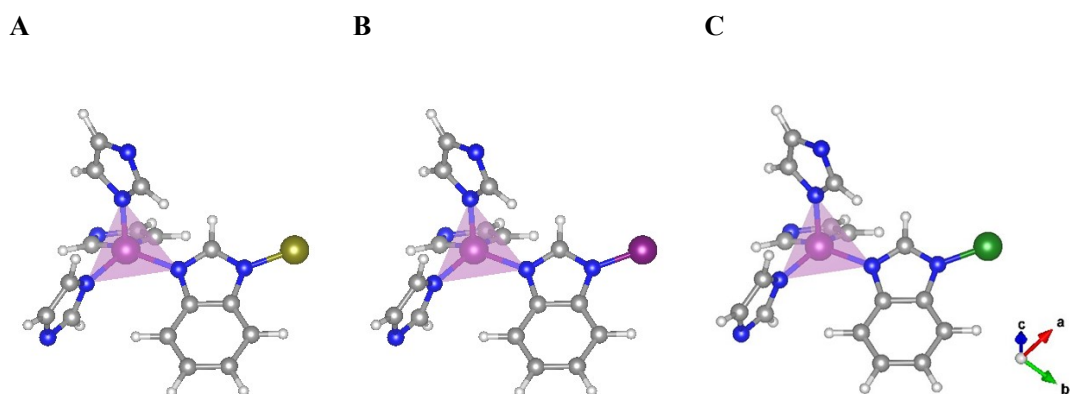
Figure S3 Models used in the DFT calculations: (A) ZIF-62(Co)-Fe; (B) ZIF-62(Co)-Co; (C) ZIF-62(Co)-Ni. White spheres: hydrogen; grey spheres: carbon; blue spheres: nitrogen; purple spheres: cobalt; gold spheres: iron; green spheres: nickel.
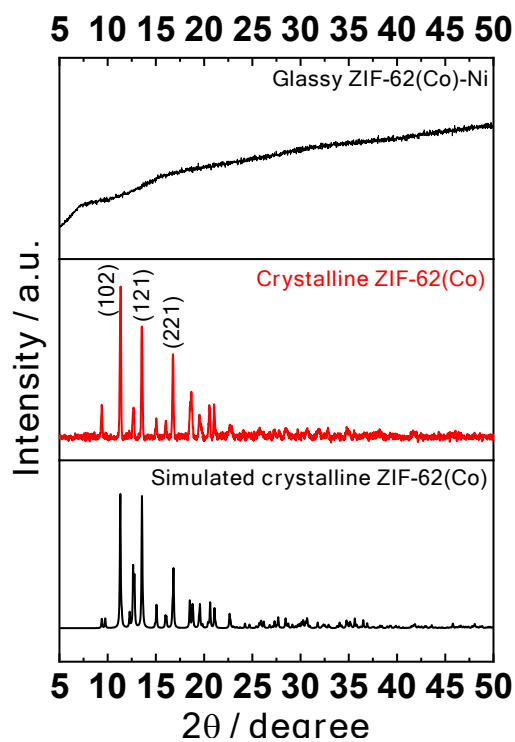

Figure S4 XRD pattern of glassy ZIF-62(Co)-Ni. The experimental and simulated results of the crystalline ZIF-62(Co) were also provided.
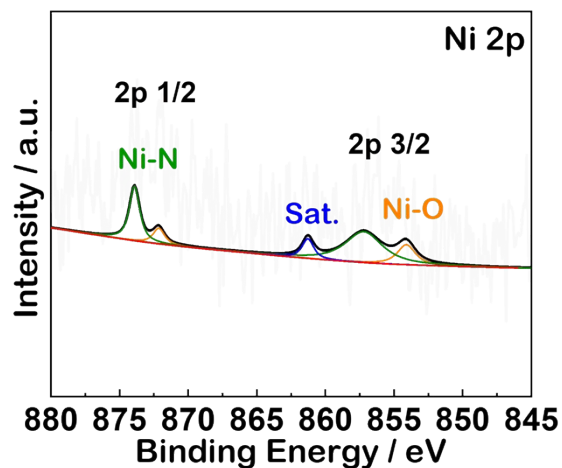
Figure S5 High-resolution Ni 2p XPS spectrum of the glassy ZIF-62(Co)-Ni.
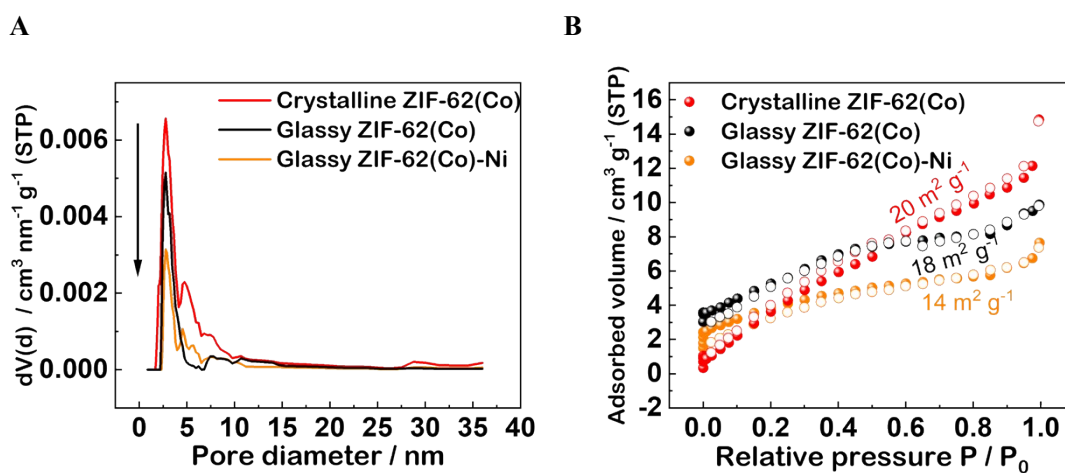
Figure S6 BET analysis for the crystalline ZIF-62(Co), glassy ZIF-62(Co), and glassy ZIF-62(Co)-Ni. (A) BJH pore size distribution and (B) N_2 adsorption and desorption isotherms.
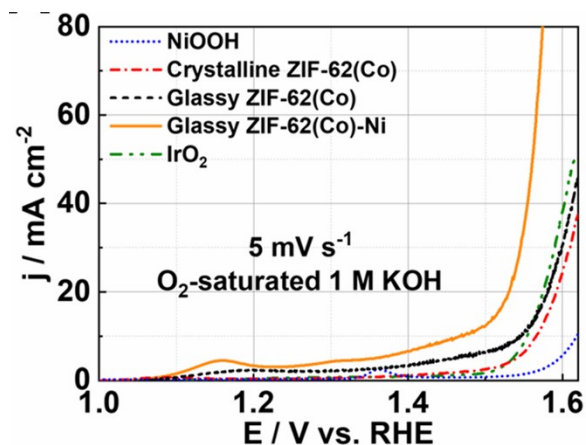
Figure S7 LSV curves of crystalline ZIF-62(Co), glassy ZIF-62(Co), glassy ZIF-62(Co)-Ni, NiOOH, and IrO$_2$, measured in O$_2$-saturated 1 M KOH at a scan rate of 5 mV s^{-1}. Note that the LSV measurements shown here were performed from low to high potential, while those in Figure 4 A were performed from high to low potential to avoid the possible oxidation effects.
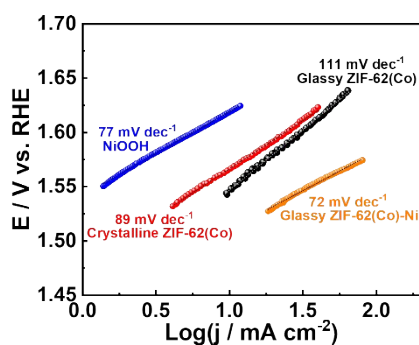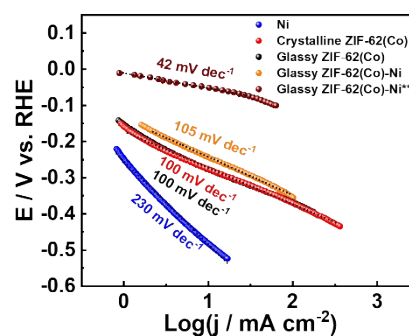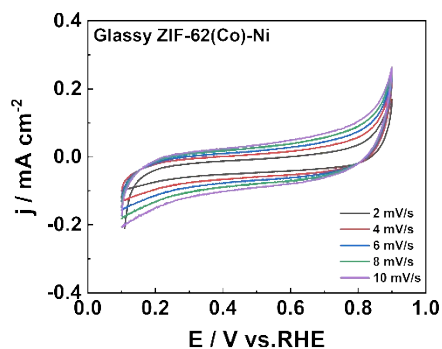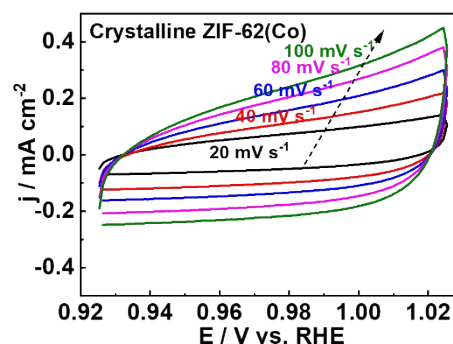

Figure S8 Tafel slopes calculated of glassy ZIF-62(Co)-Ni electrodes used for OER (A) and HER (B). The values obtained of crystalline ZIF-62(Co), glassy ZIF-62(Co), NiOOH, and Ni were also given for comparison.
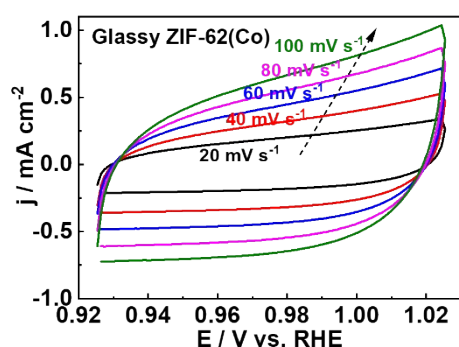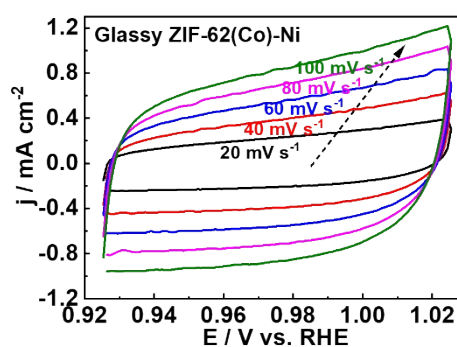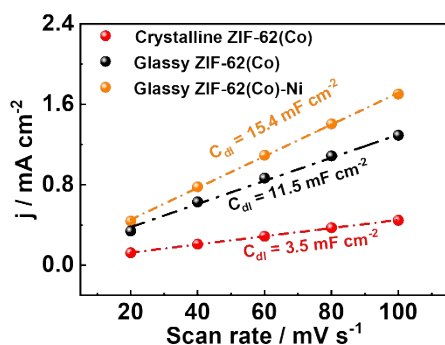
Figure S9 (A) CV curves of glassy ZIF-62(Co)-Ni in a non-Faradaic region at the scan rates of 2, 4, 6, 8, and 10 mV s^{-1}. CV curves of crystalline ZIF-62(Co) (B), glassy ZIF-62(Co) (C), and glassy ZIF-62(Co)-Ni (D) at the scan rates of 20, 40, 60, 80, and 100 mV s^{-1}.
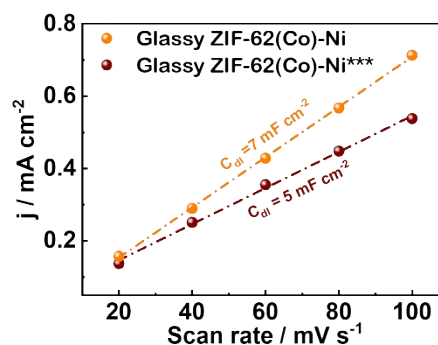

Figure S10 (A) Dependence of capacitive current on scan rates of crystalline ZIF-62(Co), glassy ZIF-62(Co), and glassy ZIF-62(Co)-Ni electrodes. (B) Dependence of capacitive current on scan rates of glassy ZIF-62(Co)-Ni and glassy ZIF-62(Co)-Ni*** electrodes with a nickel content of 0.5 and 1.9 wt.% after increasing the melting time to 1 h.
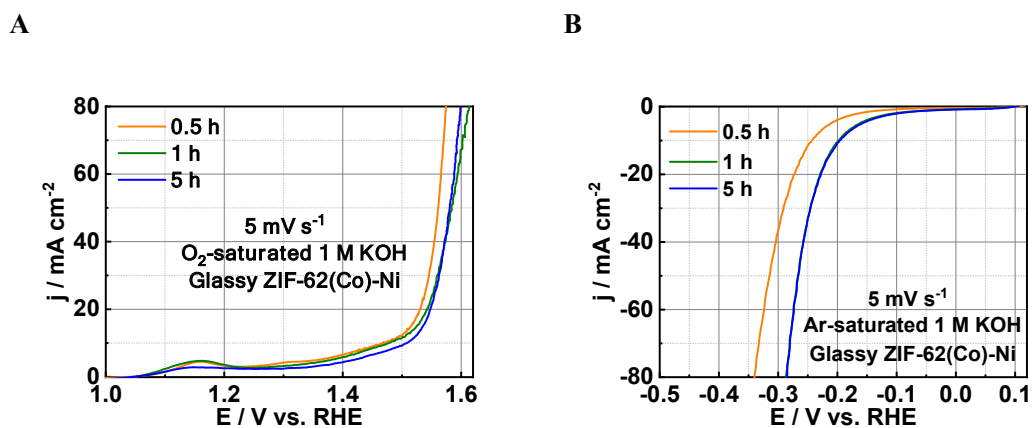
Figure S11 (A) OER and (B) HER performance of glassy ZIF-62(Co)-Ni with varied melting times at a thermal temperature of 475 °C. Note that the curve of 1 h is overlapped with that of 5 h in Figure B.
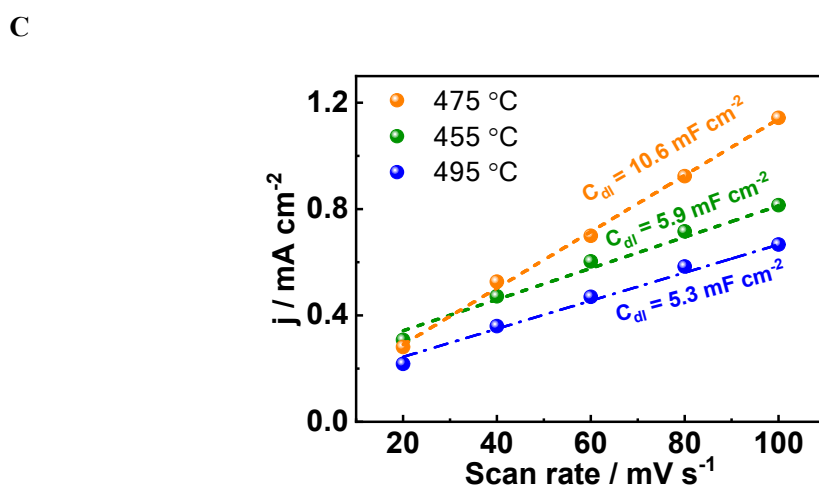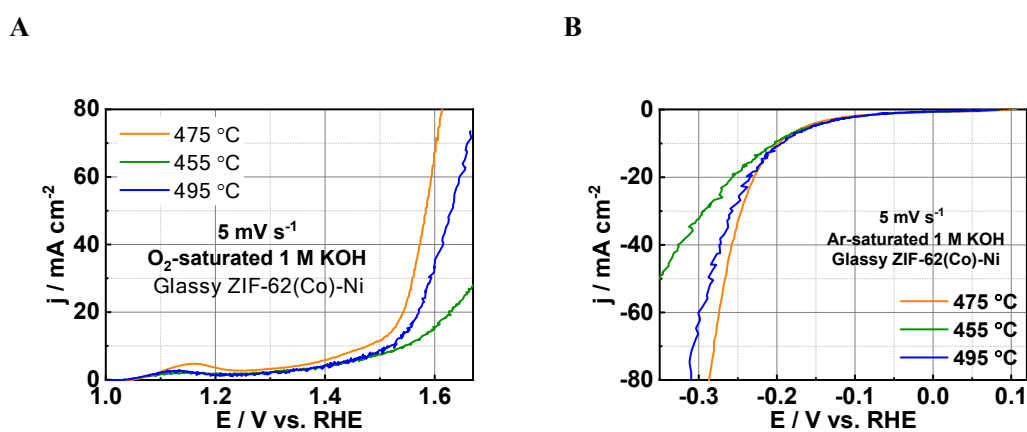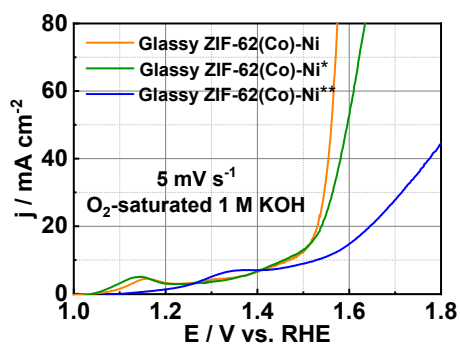

Figure S12 (A) OER and (B) HER performance of glassy ZIF-62(Co)-Ni with varied melting temperatures. Note that the melt times selected for ZIFs towards OER and HER were 0.5 h and 1 h, respectively. (C) Dependence of capacitive current on scan rates of glassy ZIF-62(Co)-Ni electrodes with varied melting temperatures.
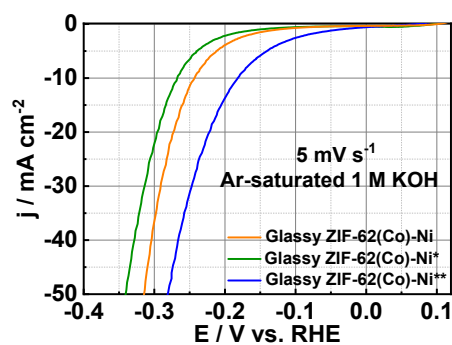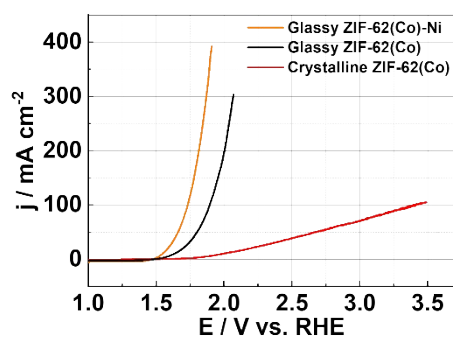
A

B

Figure S13 (A) OER and (B) HER performance of glassy ZIF-62(Co)-Ni with varied nickel doping amounts. The Nickel mass content in glassy ZIF-62(Co)-Ni*, glassy ZIF-62(Co)-Ni, and glassy ZIF-62(Co)-Ni** were 0.1, 0.5, and 0.8 wt. %, according to the ICP-MS analysis (Table S1). Note that the melt time and temperature selected for ZIFs are 0.5 h and 475 °C, respectively.
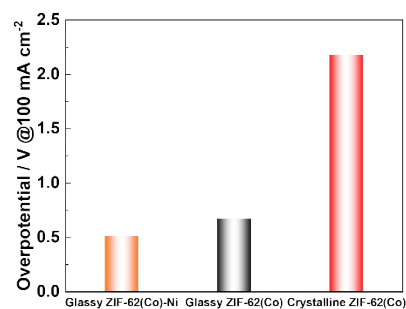
A

B

Figure S14 (A) Polarization curves of glassy ZIF-62(Co)-Ni, glassy and crystalline ZIF-62(Co) for catalyzing overall water splitting in Ar-saturated 1 M KOH at a scan rate of 5 mV s^{-1}. (B) Corresponding overpotential comparison for overall water splitting at a current density of 100 mA cm^{-2}.
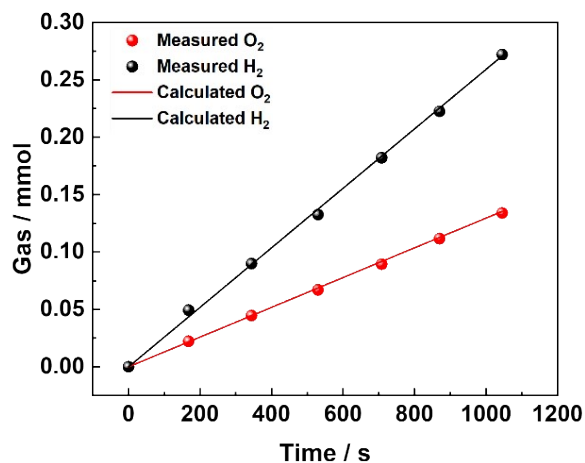
Figure S15 Measured O_2 and H_2 yields using Archimedes' method. Solids lines represent the gas evolution at 100% Faradaic efficiency.
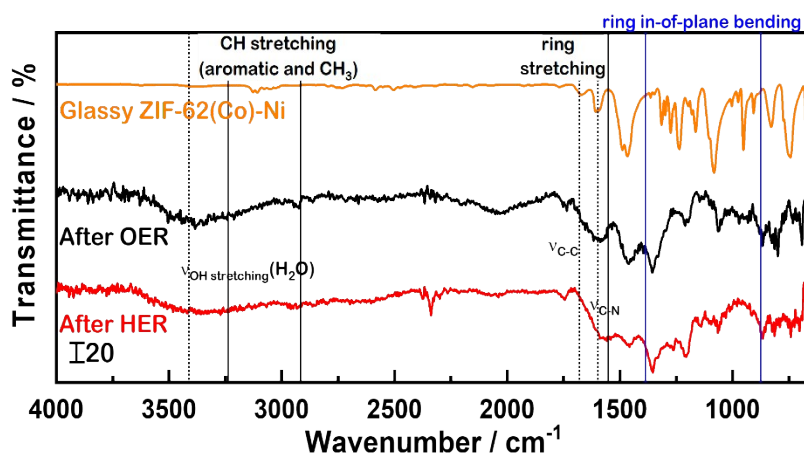

Figure S16 FT-IR spectra of the glassy ZIF-62(Co)-Ni electrodes after OER and HER, in which the origin one was also given.
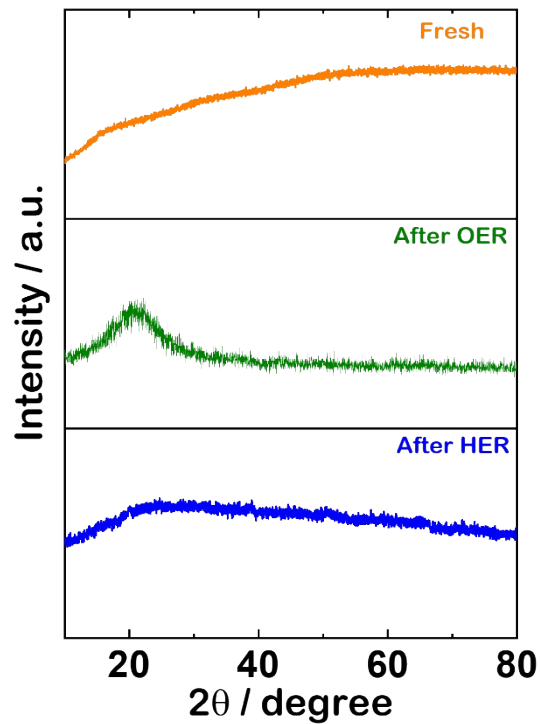
Figure S17 XRD patterns of anodic and cathodic glassy ZIF-62(Co)-Ni after the AST. The fresh glassy ZIF-62(Co)-Ni spectrum was also shown for comparison.
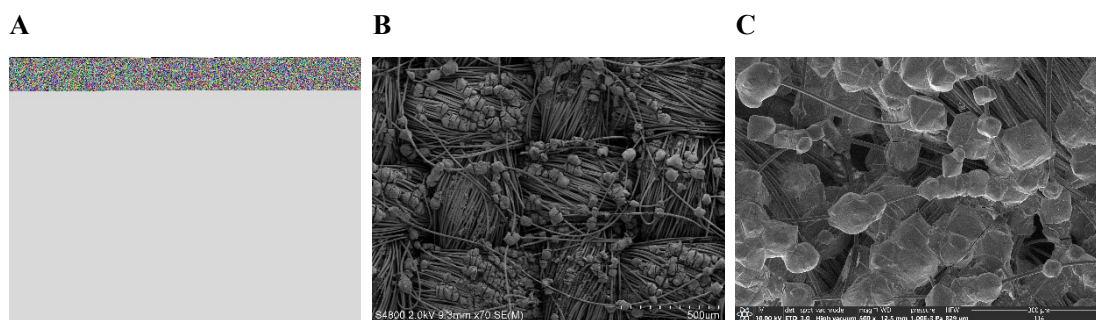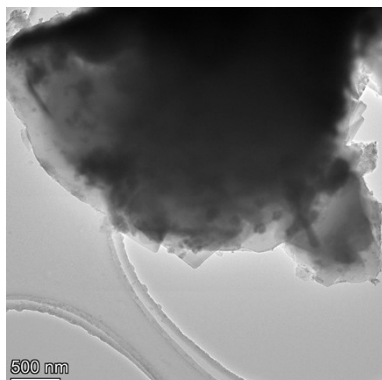

Figure S18 SEM image of the crystalline ZIF-62(Co) (A), after OER (B), and after HER (C).
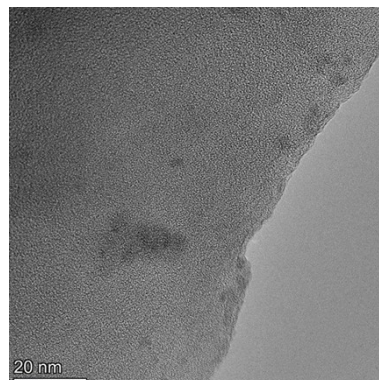
A   B
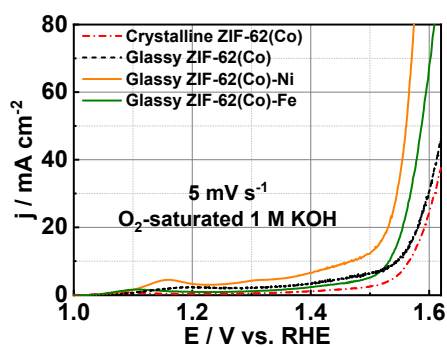

Figure S19 TEM images of the anodic glassy ZIF-62(Co)-Ni after the AST. No obvious corrosion was observed.
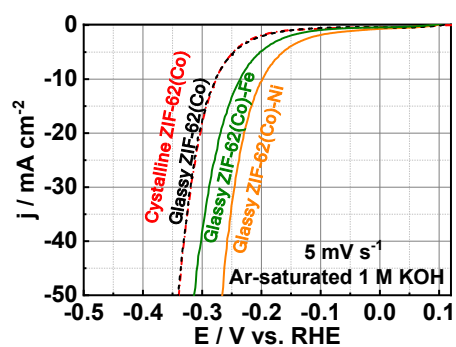
A   B

Figure S20 (A) OER and (B) HER performance of the glassy ZIF-62(Co)-Fe. The preparation procedure of the glassy ZIF-62(Co)-Fe was similar to that of the glassy ZIF-62(Co)-Fe, but the iron nitrate was used to replace nickel nitrate. The melt temperature was 475 °C. The melt time for OER electrodes was 0.5 h, while for HER electrodes was 1 h. The activities of the glassy ZIF-62(Co)-Ni, glassy ZIF-62(Co), and crystalline ZIF-62(Co) were also given for comparison.
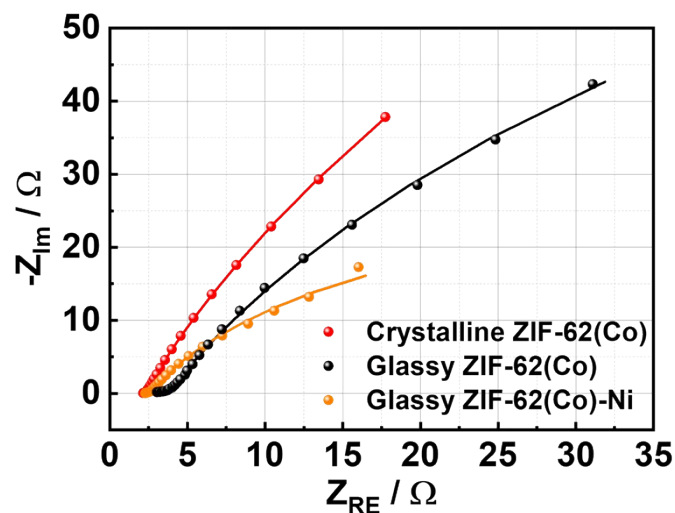
A
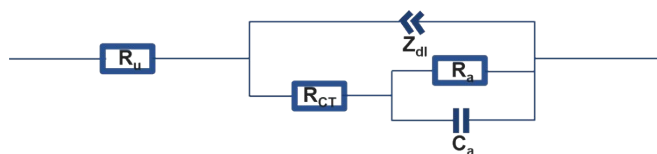
B

Figure S21 (A) Equivalent electric circuit used for fitting the obtained impedance results in all of the measurements. R_u represents the uncompensated resistance of the electrolyte; Z_{dl} the double layer capacitance; R_{ct} charge transfer resistance; R_a adsorption resistance; C_a adsorption capacitance. (B) Nyquist plots of crystalline ZIF-62(Co), glassy ZIF-62(Co), and glassy ZIF-62(Co)-Ni obtained at a potential of ~0.93 V_{RHE}. Void and solid curves are original and fitting data, respectively.
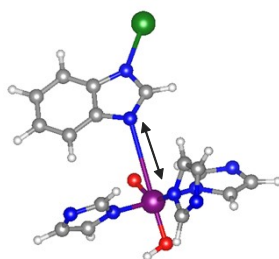

Figure S22 Atomic configuration of OOH adsorbed on the Co site of the glassy ZIF-62(Co)-Ni. The (benz)imidazole binding was somewhat weakened, likely resulting in the characteristic peak of imidazole shifting to lower wavenumbers as well as weakening.
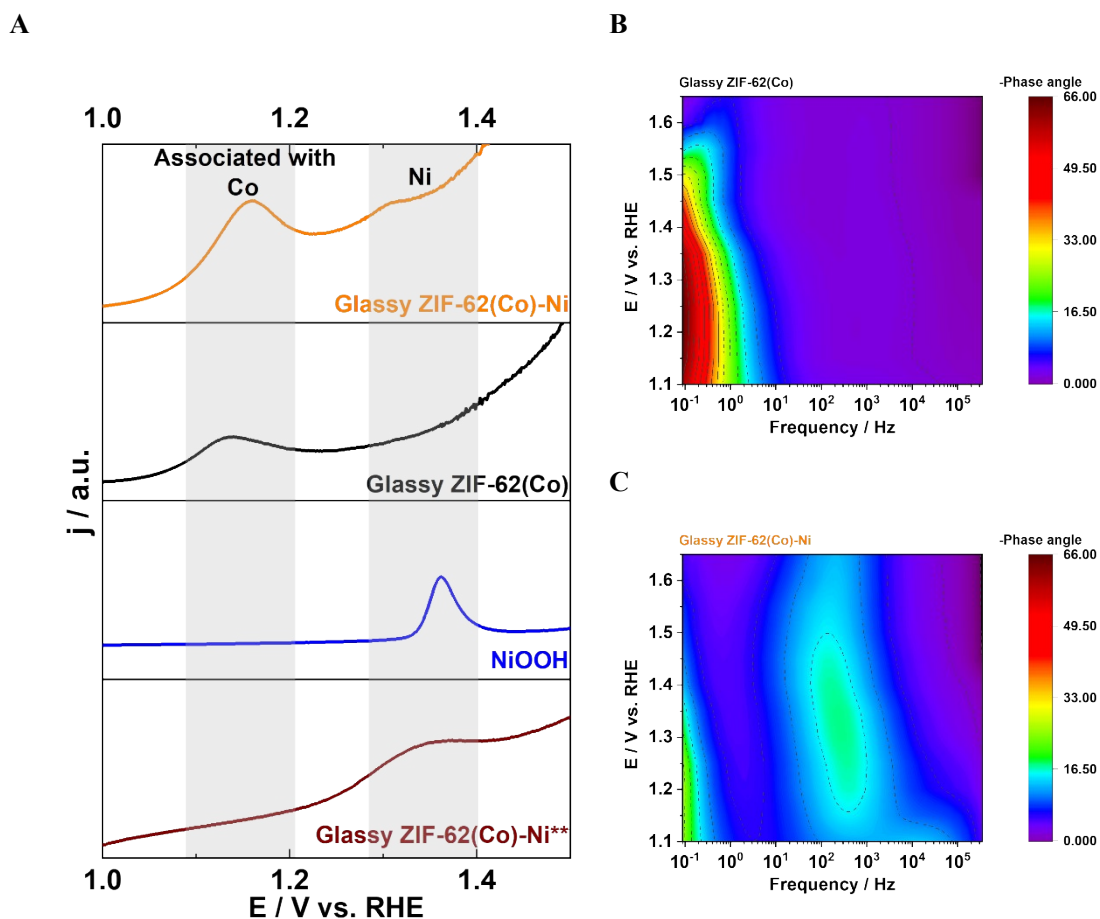
Figure S23 (A) Voltammograms for glassy ZIF-62(Co)-Ni, glassy ZIF-62(Co), NiOOH, and glassy ZIF-62(Co)-Ni** in 1 M KOH at a scan rate of 5 mV s^{-1}. Operando electrochemical impedance spectroscopy (EIS) on (B) glassy ZIF-62(Co) and (C) glassy ZIF-62(Co)-Ni in 1 M KOH at applied potentials from 1.1 to 1.65 V$_{RHE}$.
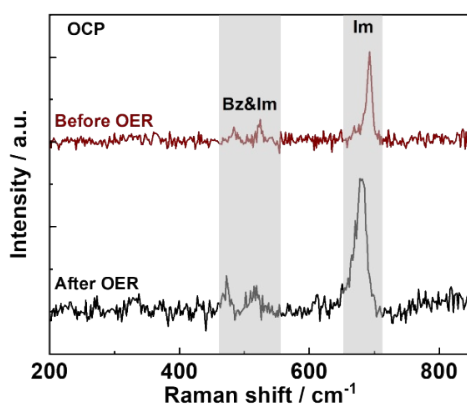

Figure S24 *In-situ* Raman spectra of glassy ZIF-62(Co)-Ni at open circuit potential (OCP) before and after OER.
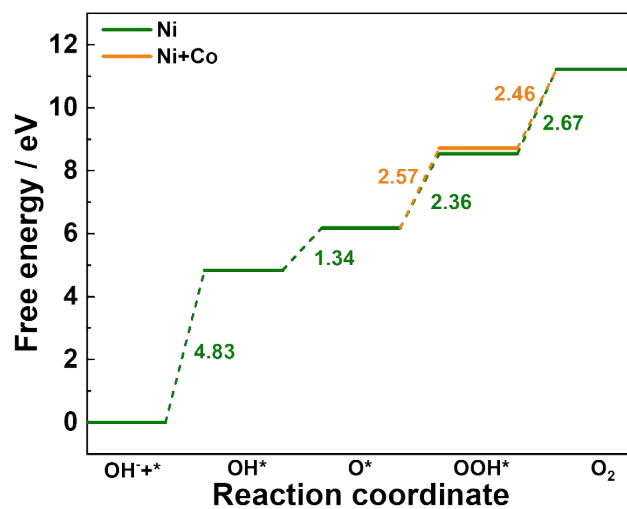
Figure S25 Free energy diagram for OER on Ni+Co and Ni sites. Note that the DFT calculation for the Ni+Co sites was intricate. Thus, the hydroxyl spillover was assessed by accounting for the formation of hydroxyl radicals and adsorbed OOH, elucidating its impact on Step III.
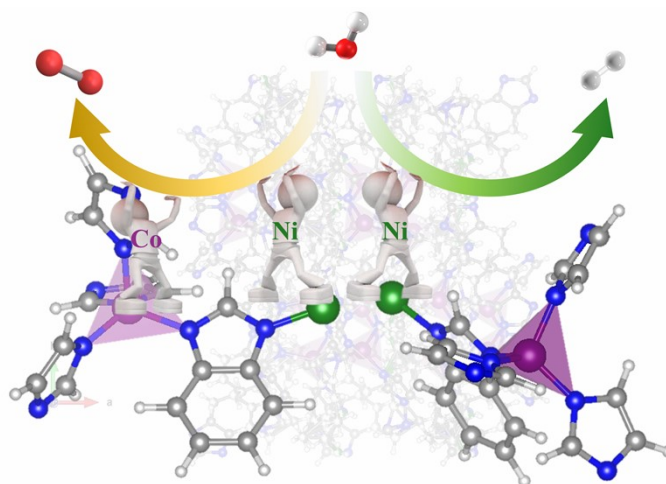

Figure S26 Bimetallic functionality proposed on the glassy ZIF-62(Co)-Ni towards oxygen and hydrogen evolution.

Table S1. Nickel mass content in ZIF-62(Co)-Ni with varied nickel doping amounts using the ICP-MS.

Samples	Ni (wt. %)
ZIF-62(Co)-Ni*	0.1
ZIF-62(Co)-Ni	0.6
ZIF-62(Co)-Ni**	0.9
ZIF-62(Co)-Ni***	1.9